

Enhanced Airborne Optical Sectioning Design via HSV Color Space for Detecting Human Object Under Obscured Aerial Image Environment

KangSoo Ryu, Byungjin Lee, Dong-Gyun Kim, and Sangkyung Sung*

Abstract: This paper aims to develop an algorithm to identify the obscured target from the aerial image encountered in a general complex flight environment. For this, an airborne optical sectioning (AOS) and synthesizing technique is newly adapted for the purpose of preliminary data processing. Specifically, the proposed algorithm consists of several image processing stages. In a foliage-rich environment, the majority of an image may be occupied by trees, where it is difficult to detect a person hidden under foliage. To resolve this, the preprocessing stage in the HSV color space removes the tree parts while preserving the person, and the processed images are combined to construct the AOS, which reveals the person hidden under the trees. Then the exposed person is identified using the machine learning technique that accurately recognizes human shapes. Consequently, the proposed optical sectioning and synthetic process suggests to expand the application field of typical vision-based mission system under complex airborne environment. The performance of the proposed algorithm is demonstrated through the airborne data from a high fidelity process-in-the-loop simulator, where sensor and vision measurement are constructed and provided to a level of practical flight environment.

Keywords: Aerial image, airborne optical sectioning, high-fidelity simulator, machine learning, vision-based mission system.

1. INTRODUCTION

Recently, various studies have been conducted on how to use aerial photography images. These include a landing guidance system of unmanned aerial vehicles with deep learning [1], a vision navigation system using multi matching images referenced by stored map tiles, which can be used on unmanned aerial vehicle [2]. Moreover, the research on aerial photography using the drone's versatility also has been active: the effective target search mechanism using the downward-facing cameras mounted on drones [3], helping unmanned ground vehicles recognize obstacles that can lead to mission failure [4], for instance. Along with this, the airborne optical sectioning (AOS) is a useful synthetic aperture imaging technique that can be used on aerial images captured by drones and other aerial mechanisms [5]. It is reported the system can effectively imitate the wide-aperture optics of the scan area's size and shape (e.g., hundreds to thousands of square meters), resulting in images of extremely shallow depths over the enclosed environments such as forests. These images are created by combining multiple individual photos taken by

the drone in different spots, allowing for optical slicing through dense surroundings with leaves, branches, and bushes. As the AOS could reveal objects that are concealed by normal cameras in each slice, such as artifacts, objects, wild animals, or humans, it has been widely employed in the disciplines of archaeology, wildlife observation [6], and search and rescue (SAR) application [7–9], where numerous outcomes were successfully achieved. In these studies, it was shown that classifying the partially obscured identities from thermal images in a forest environment was considerably more effective than classifying partially obscured identifiers in a single image, when applying AOS to aerial thermal imaging. Researchers also showed how the AOS could be used in fully autonomous and classification-driven adaptive SAR operations in real-time cases. In the same study, average precision scores in the IR spectrum ranged from 86.0 to 92.2 percent.

Even though the AOS method is shown to have efficiency in the SAR application, however, it is mostly based on thermal image measurement. Exceptionally, a study using vision image is reported, but it is only applied to observe animals over the tree. Thus this proves it is still very

Manuscript received August 18, 2022; revised April 18, 2023 and July 6, 2023; accepted August 9, 2023. Recommended by Associate Editor Ning Sun under the direction of Senior Editor Chan Gook Park. This research was funded by the Korean National Research Fund (NRF-2022R1A2C1005237), the Unmanned Vehicles Core Technology Research and Development Program through the National Research Foundation of Korea (NRF-2020M3C1C1A01086408) and the MSIT(Ministry of Science and ICT), Korea, under the ITRC(Information Technology Research Center) support program(IITP-2023-2018-0-01423) supervised by the IITP.

KangSoo Ryu, Byungjin Lee, Dong-Gyun Kim, and Sangkyung Sung are with the Department of the Aerospace Information Engineering, Konkuk University, 120 Neungdong-ro, Gwangjin-gu, Seoul, Korea (e-mails: {rksa1234, schumir, kdgyun88, sksung}@konkuk.ac.kr).

* Corresponding author.

difficult to completely detect and localize the obscured SAR objects such as human under the high and dense trees. In other words, to employ AOS in the current SAR field, expensive and heavy thermal imaging equipment is required, which limits the drone's mission sustainability.

Meanwhile, researches for processing image pixels composed of the visible ray's color space has been conducted by mostly utilizing a variety of color spaces, including the hue, saturation, and value (HSV) and YCbCr in addition to the typical RGB color space [10-13]. In particular, a study used the characteristics of each parameter of hue, saturation, and value (i.e., brightness) of the HSV color space instead of the typical RGB region to accomplish feature extraction for image segmentation [10]. In addition, instead of simply adapting the RGB color space, researchers used the hue and brightness characteristics in the HSV color space to detect objects whose properties change depending on areas, individuals, or lighting conditions, such as human skin [11]. And HSV color space can be used in the video-surveillance and traffic analysis systems for detecting and suppressing shadows of moving objects to enhance localization, detection of vehicle or pedestrians [12]. Furthermore, there is a research about denoising and enhancement methods of nonlinear HSV color models for non-flat features to denoise the chromaticity and hue components directly [13]. Despite the advantages of using hue and brightness in visual identification problem, its application to search and rescue problem specifically under an obscured aerial environment is not reported within the scope of author's knowledge.

In this background, this research aims to develop an algorithm that uses the characteristics of the HSV color space to analyze and process the aerial images from a forest environment where survivors are obscured by trees. For this, an overall framework integrating the image processing algorithm and optical sectioning and synthetic procedure is designed. Considering a practical onboard application, a navigation result employing a control-grade inertial measurement unit (IMU) is adopted to provide pose information required during the AOS synthetic procedure. As a result, it was suggested the drone's AOS-based SAR mission could be carried out even when only a lightweight vision camera is used instead of an expensive and heavy thermal imaging equipment. For the performance verification, a high fidelity simulator is employed, where the real vegetation environment and realistic sensor measurements were generated for comparing with the reference identification ratio.

2. AIRBONE OPTICAL SECTIONING TECHNIQUE

A typical airborne optical sectioning (AOS) creates a large artificial aperture of 30 m-100 m in diameter by using synthetic aperture imaging to sample optical data from

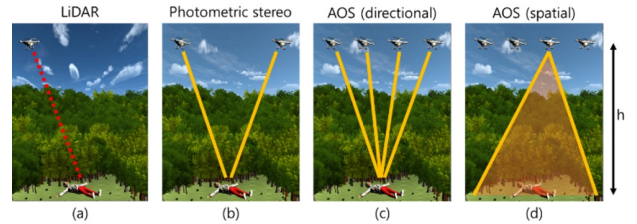


Fig. 1. Schematics of observing ground target under occlusion.

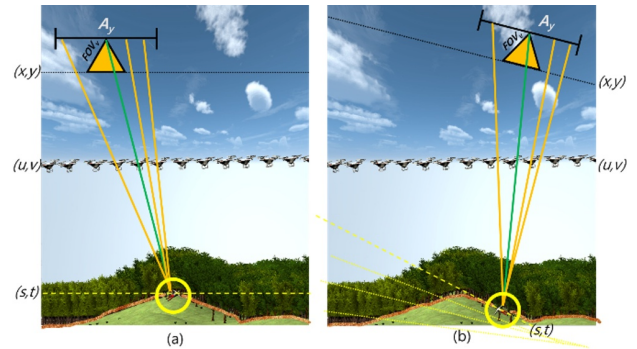


Fig. 2. Synthetic aperture of virtual camera and visualization.

different angles and adjusting the depth of field to focus solely on the desired object, such as a survivor, and other objects. Even in densely forested locations, dense trees can be ignored and ground targets recognized by defocusing and blurring.

The existing approach is compared to AOS in Fig. 1. Depth to the ground and point clouds of image features can be set using a single view in LiDAR (a) and photometric stereo (b). There are drawbacks, such as the difficulty in securing information and lengthy computation time it takes. As a result, AOS may create optical sectioning with a low synthetic focal length by combining several acquired images (c) obtained from various angles relative to the synthetic focal plane. The spatial sampling density of the focal plane is determined by the drone camera's field of view (FOV), resolution, and the drone's height relative to the focal plane (d).

Fig. 2 shows a virtual camera and visualization for the Synthetic Aperture that has been configured. A virtual camera (yellow triangle) can be defined for each pose, aperture size, the field of view, and focal plane output as a result of air navigation to visualize navigation objects. Ray integration is used to create a new image for point (s,t) in the focal plane (yellow circle), which is defined as the intersection of the camera's projection center (gray circle) and the ray passing through (x,y) pixels on the image plane (green). Within the field of view FOV_v , pixels (x,y) are in the camera image plane (green circles). Only ray (yellow) traveling through (u,v) is included in the vir-

tual camera's synthetic aperture plane via the aperture Av. (a) depicts a single focal plane visualization, and (b) depicts focal slicing by the depth of field. A wide aperture may be made to get an image of each depth of the subject. So, by adjusting the focal length, blurring obstacles such as trees and other ground objects that are not in the focal plane, and clearly revealing only objects such as important survivors.

3. ENHANCED AOS INTEGRATION SYSTEM WITH HSV PRE-PROCESSED IMAGE

3.1. HSV color anomaly detection processing

The theoretical background of finding survivors using the AOS has been properly validated, as mentioned in the previous section. However, shadows cast by dense trees in the forest usually cover objects on the ground under the forest when images are taken from the aerial vehicle. Thus if the AOS only employs RGB images and doesn't use thermal imaging equipment, the ground image is simply dark and cannot be processed properly. Furthermore, even when the focal length is adjusted with the AOS, it is blurred rather than excluded as shown in Fig. 3. Hence, contrary to the AOS's goal, the wood sections in most images become more dominant, and the ground part between leaves and branches gets less clear in combined images.

Therefore, before using the AOS, a pre-processing step is required, and the image processing step in the HSV color space is newly implemented in this study.

The upper left image of Fig. 4 shows a drone flying through a forest where a troubled individual can be found.

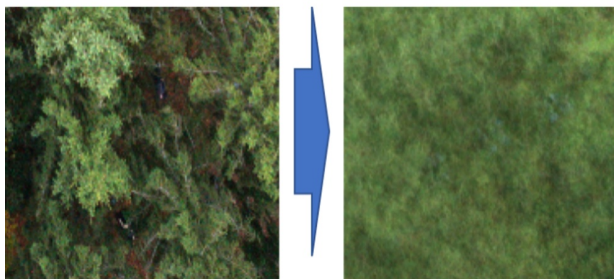


Fig. 3. Limitations of traditional RGB-based AOS.

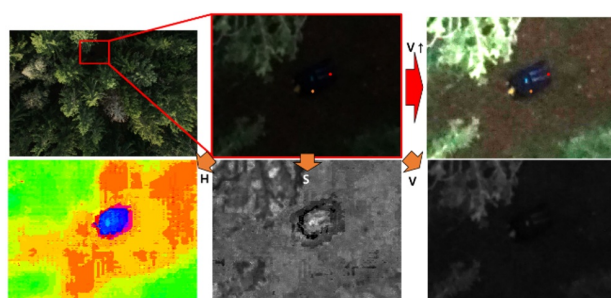


Fig. 4. HSV analysis of actual forest environment image.

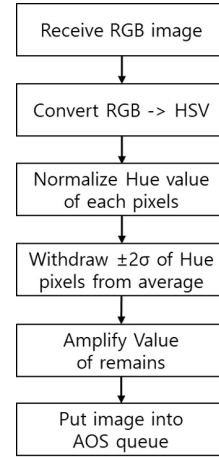


Fig. 5. HSV pre-process algorithm flowchart.

The enlarged image around human as shown in the upper middle subplot is displayed in almost black by the shadow of the tree, despite an enlarged image distress. When the image is decomposed into hue, saturation, and value (i.e., brightness), it can be seen that, even if the image is dark due to shadows, the hue and saturation values preserve the characteristics of the primary colors before shadows, and only the brightness is low (as shown in the lower subplots). Therefore, when the brightness of that section is increased, the part covered by the shadow is revealed as shown in the upper right subplot of Fig. 4, and the distress on the ground can be recognized. According to the hue value, the green spectrum section indicates leaves/grass, while the yellow spectrum part represents tree poles/twigs/fallen leaves. When these green spectrum of hue value pixels are removed, only the survivors can be distinguished.

The proposed pre-processing is represented in Fig. 5, which is based on the concept that is previously mentioned. The RGB image sensor's output is first converted to HSV color space. Next, the hue values of each pixel in the image are normalized, as illustrated in Fig. 6. A hue distribution close to the normal distribution is illustrated in the case of a natural environment such as a general forest, as shown in Fig. 6, with the average hue value composed of the forest's primary trees. Therefore, if 2σ (95 percent) cut-off criterion is applied to the approximated hue normal distribution, the primary trees that make up a large portion of the aforementioned images can be removed, where only the ground image remains in an effective way.

If there is a shadow cast by dense trees on the ground, where it is difficult to identify the troubled person in black shades, the brightness value of the remaining ground can be boosted to remove the shadow shading. If the AOS is applied based on the collected ground photos, it is possible to successfully discover survivors who were concealed by trees and shadows that did not appear in the AOS without this pre-processing. Consequently, with the proposed image processing, it is possible to overcome the constraints

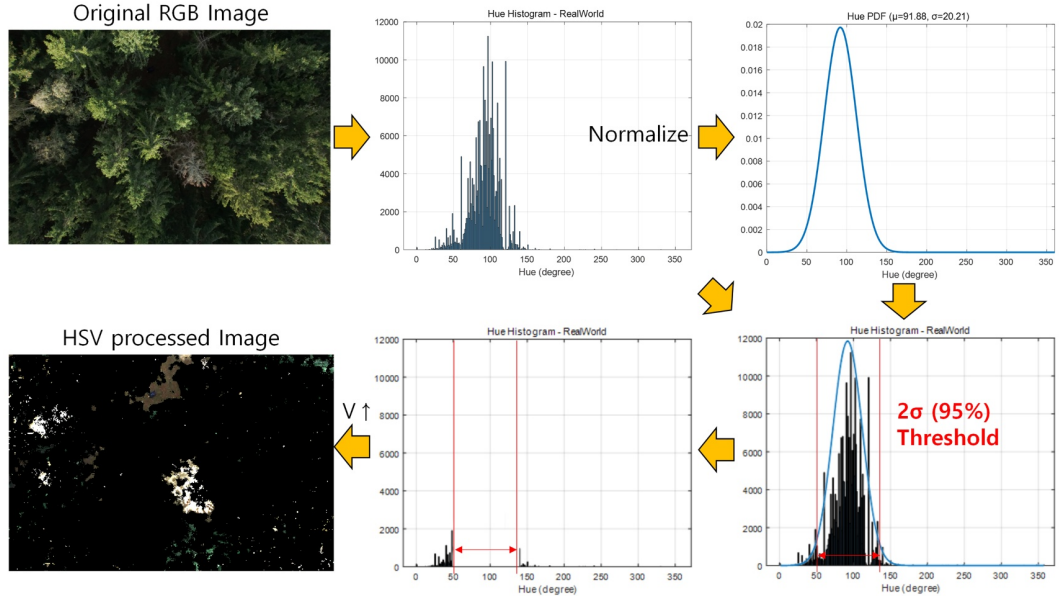


Fig. 6. Emphasis on survivors using HSV pre-process algorithm.

of tree occlusion in the visible light area and to search for survivors on the ground without complicated formulas.

One notable exception to the challenges of HSV based color anomaly detection is an environment with achromatic colors, such as a forest covered in snow during winter. Snow may appear white and have a low saturation value, making it difficult to determine its hue. However, a snow-covered forest has a blue tint due to the reflection of a blue skylight. This phenomenon is illustrated in Fig. 7. So the HSV-enhanced AOS algorithm proposed in this paper operates effectively in all environments, including those with achromatic colors, by utilizing the characteristics mentioned above. These characteristics have been applied in the simulation presented in this study.

3.2. Enhanced AOS via HSV preprocessing with low-cost navigation system

In implementing the AOS, the position and attitude when the aerial image is generated are critical to the detection performance. Therefore, an onboard navigation system including practical inertial sensor, GNSS receiver, and barometer is configured for evaluating the real performance analysis and demonstration of the proposed algorithm. For this, an INS/GNSS/Baro loose-coupled EKF is implemented by defining the following 16 states of states [14].

$$x = [\mathbf{P}^T \ \mathbf{V}^T \ \mathbf{q}^T \ \mathbf{b}_a^b \ \mathbf{b}_g^b]^T. \quad (1)$$

Equation (1) shows the simple INS state in this paper. \mathbf{P} means position, \mathbf{V} is velocity, \mathbf{q} is quaternion attitude from N -frame, respectively. And additionally, \mathbf{b}_a^b is accelerometer bias and \mathbf{b}_g^b is gyroscope bias, where navigation accuracy and filter stability are improved through sensor noise

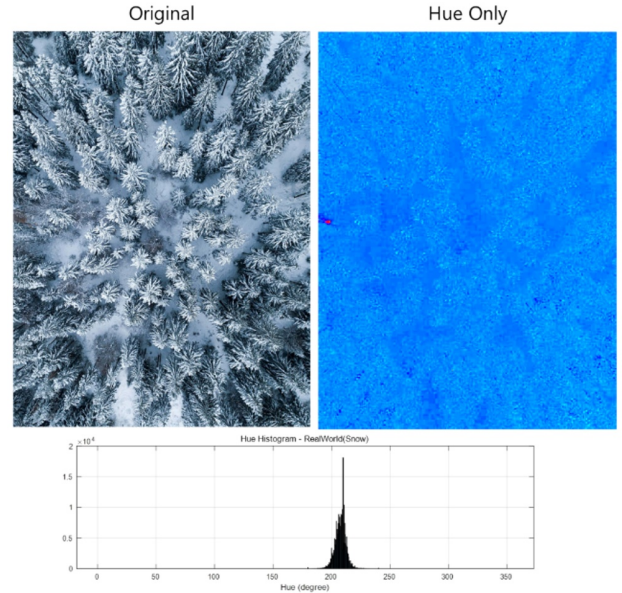


Fig. 7. Real snow-covered forest environment Hue analysis.

estimation.

$$\bar{\mathbf{x}}_k = \mathbf{f}(\mathbf{x}_{k-1}, \mathbf{u}) = \begin{bmatrix} \mathbf{P}_{k-1} + \mathbf{V}_{k-1} \cdot \Delta t + \frac{\mathbf{a}_n \cdot (\Delta t)^2}{2} \\ \mathbf{V}_{k-1} + \mathbf{a}_n \cdot \Delta t \\ \mathbf{q}_{k-1} + \frac{d\mathbf{q}_{k-1}}{dt} \cdot \Delta t \\ \mathbf{b}_{a,k-1}^b \\ \mathbf{b}_{g,k-1}^b \end{bmatrix}, \quad (2)$$

where

$$\mathbf{u} = \begin{bmatrix} \mathbf{A}_b \\ \vec{\omega}_b \end{bmatrix}_{6 \times 1} \equiv [\mathbf{A}_x \ \mathbf{A}_y \ \mathbf{A}_z \ \mathbf{p} \ \mathbf{q} \ \mathbf{r}]^T,$$

$$\begin{aligned}\mathbf{A}_b &= Acc - \mathbf{b}_a^b, \quad \omega_b = Gyro - \mathbf{b}_g^b, \\ \mathbf{a}_n &= \mathbf{C}_b^n \cdot \mathbf{A}_b - [\mathbf{0} \ \mathbf{0} \ -\mathbf{G}]^T.\end{aligned}$$

Equation (2) shows INS propagation. In this simulation, low cost IMU of MEMS grade is used by considering on-board drone application, so the effects of earth rotation and frame rotation are ignored. Thus, the Jacobian of \mathbf{x}_k^- by \mathbf{x}_{k-1} and Jacobian of \mathbf{x}_k^- by \mathbf{u} are derived as (3) and (4) through the linearization of (2).

$$\begin{aligned}\frac{\delta \mathbf{x}_k^-}{\delta \mathbf{x}_{k-1}} &= \mathbf{A} \\ &= \begin{bmatrix} \mathbf{I}_{3 \times 3} & \mathbf{I}_{3 \times 3} \cdot \Delta t & \frac{\delta \mathbf{a}_n}{\delta \mathbf{q}} \cdot \frac{(\Delta t)^2}{2} \\ \mathbf{0}_{3 \times 3} & \mathbf{I}_{3 \times 3} & \frac{\delta \mathbf{a}_n}{\delta \mathbf{q}} \cdot \Delta t \\ \mathbf{0}_{4 \times 3} & \mathbf{0}_{4 \times 3} & \mathbf{I}_{4 \times 4} + \frac{1}{2} \cdot \begin{bmatrix} 0 & -p & -q & -r \\ p & 0 & r & -q \\ q & -r & 0 & p \\ r & q & -p & 0 \end{bmatrix} \cdot \Delta t \\ \mathbf{0}_{3 \times 3} & \mathbf{0}_{3 \times 3} & \mathbf{0}_{3 \times 3} \\ \mathbf{0}_{3 \times 3} & \mathbf{0}_{3 \times 3} & \mathbf{0}_{3 \times 3} \\ -\frac{\mathbf{C}_b^n \cdot (\Delta t)^2}{2} & \mathbf{0}_{3 \times 3} & \mathbf{0}_{3 \times 3} \\ -\mathbf{C}_b^n \cdot \Delta t & \mathbf{0}_{3 \times 3} & \mathbf{0}_{3 \times 3} \\ \mathbf{0}_{4 \times 3} & -\frac{1}{2} \cdot \begin{bmatrix} -q_1 & -q_2 & -q_3 \\ q_0 & -q_3 & q_2 \\ q_3 & q_0 & -q_1 \\ -q_2 & q_1 & q_0 \end{bmatrix} \cdot \Delta t & \mathbf{0}_{3 \times 3} \\ \mathbf{I}_{3 \times 3} & \mathbf{0}_{3 \times 3} & \mathbf{I}_{3 \times 3} \\ \mathbf{0}_{3 \times 3} & \mathbf{I}_{3 \times 3} & \mathbf{0}_{3 \times 3} \end{bmatrix}, \quad (3)\end{aligned}$$

where

$$\begin{aligned}\frac{\delta \mathbf{a}_n}{\delta \mathbf{q}} &= \frac{\delta (\mathbf{C}_b^n \cdot \mathbf{A}_b)}{\delta \mathbf{q}} \\ &= 2 \cdot \begin{bmatrix} -q_1 & q_0 & -q_3 & q_2 \\ -q_2 & q_3 & q_0 & -q_1 \\ -q_3 & -q_2 & q_1 & q_0 \end{bmatrix} \\ &\cdot \begin{bmatrix} 0 & -A_x & -A_y & -A_z \\ A_x & 0 & A_z & -A_y \\ A_y & -A_z & 0 & A_x \\ A_z & A_y & -A_x & 0 \end{bmatrix}, \\ \frac{\delta \mathbf{x}_k^-}{\delta \mathbf{u}} &= \mathbf{B} \\ &= \begin{bmatrix} \frac{\mathbf{C}_b^n \cdot (\Delta t)^2}{2} & \mathbf{0}_{3 \times 3} \\ \mathbf{C}_b^n \cdot \Delta t & \mathbf{0}_{3 \times 3} \\ \mathbf{0}_{4 \times 3} & \frac{1}{2} \cdot \begin{bmatrix} -q_1 & -q_2 & -q_3 \\ q_0 & -q_3 & q_2 \\ q_3 & q_0 & -q_1 \\ -q_2 & q_1 & q_0 \end{bmatrix} \cdot \Delta t \end{bmatrix}. \quad (4)\end{aligned}$$

The observation equation for filter measurement update is arranged as follows:

$$\begin{aligned}\mathbf{z}_k &= \begin{bmatrix} GNSS_{Pos} \\ GNSS_{Vel} \\ BaroHeight \end{bmatrix}_{7 \times 1} \\ &= \mathbf{H} \mathbf{x}_k^-, \quad (5)\end{aligned}$$

where

$$\mathbf{H} = \begin{bmatrix} \mathbf{I}_{3 \times 3} & \mathbf{0}_{3 \times 3} & \cdots \\ \mathbf{0}_{3 \times 3} & \mathbf{I}_{3 \times 3} & \cdots \\ [0 \ 0 \ 1] & \mathbf{0}_{3 \times 3} & \cdots \end{bmatrix}_{7 \times 16}.$$

Then, (6) completes the extended Kalman filter equations. Here, Q and R represent process and measurement noise covariance, respectively, which can be adjusted according to the system characteristics.

$$\begin{aligned}\mathbf{P}_k^- &= \mathbf{A} \cdot \mathbf{P}_{k-1} \cdot \mathbf{A}^T + \mathbf{B} \cdot \mathbf{Q} \cdot \mathbf{B}^T, \\ \mathbf{x}_k^- &= \mathbf{f}(\mathbf{x}_{k-1}, \mathbf{u}_{k-1}), \\ \mathbf{P}_k &= \mathbf{P}_k^- - \mathbf{K}_k \cdot \mathbf{H} \cdot \mathbf{P}_k^-, \\ \mathbf{K}_k &= \mathbf{P}_k^- \cdot \mathbf{H}^T \cdot (\mathbf{H} \cdot \mathbf{P}_k^- \cdot \mathbf{H}^T + \mathbf{R})^{-1}, \\ \mathbf{x}_k &= \mathbf{x}_k^- + \mathbf{K}_k \cdot (\mathbf{z}_k - \mathbf{h}(\mathbf{x}_k^-)). \quad (6)\end{aligned}$$

In the rest of the section, an improved AOS-based algorithm that integrates the image processing with the time-synchronized navigational estimates is described in detail. Fig. 8 shows the layout of the whole flow chart of the proposed algorithm.

For implementing algorithm, a path flight along a pre-defined waypoint in the search area is performed by an unmanned aerial vehicle equipped with an RGB image sensor. The image is captured at a pre-determined location, and the navigation result at the time is stored as the image metadata. Then as suggested in Subsection 3.1, the captured image is submitted to HSV pre-processing to remove pixel values related to occlusions and to save the results that leaves only the ground details. Next, repeat this procedure until all waypoints have been reached, whereas it is checked to gather sufficient photos to identify the survivors. When the path flight completes, the AOS is performed using the pose information and metadata from the saved image. Specifically, AOS is used to convey the form of objects on the ground, and in each stored pose, a virtual camera is used to make images and continue with the machine visioning process. Consequently, the suggested method finds the survivors by using the typical YOLO algorithm to detect the human shape in each pose where the image was saved.

4. SIMULATION STUDY

4.1. Simulator design and simulation environment

A high-fidelity MATLAB simulator is used to verify the proposed algorithm, which interact with the Unity3D a popular graphics development tool [15,16]. Especially,

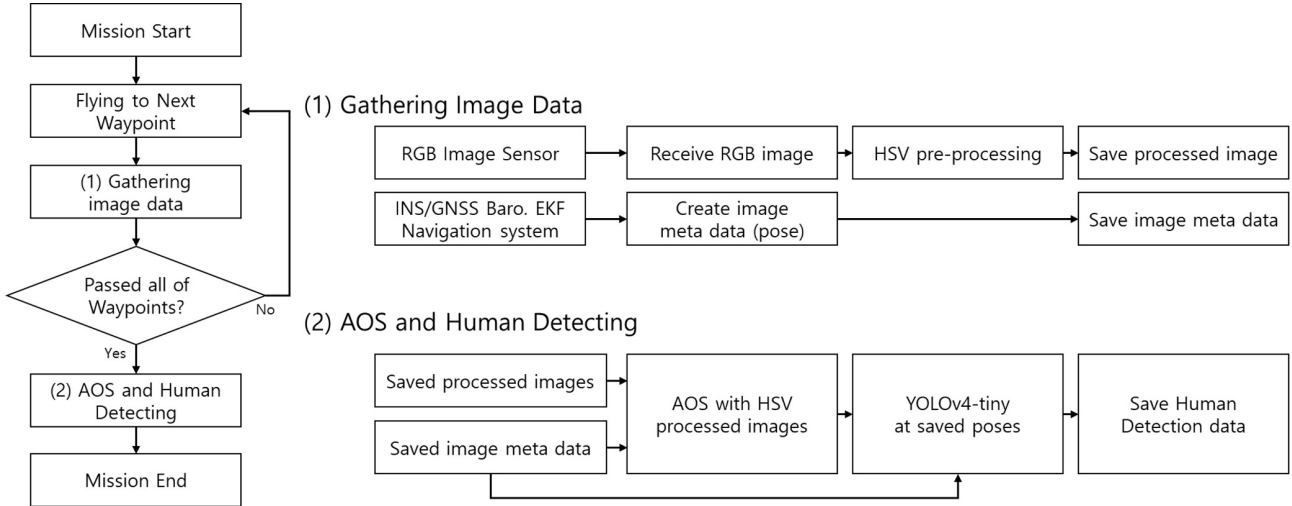


Fig. 8. Overall algorithm framework via integration of HSV preprocessing and low-cost navigation system.

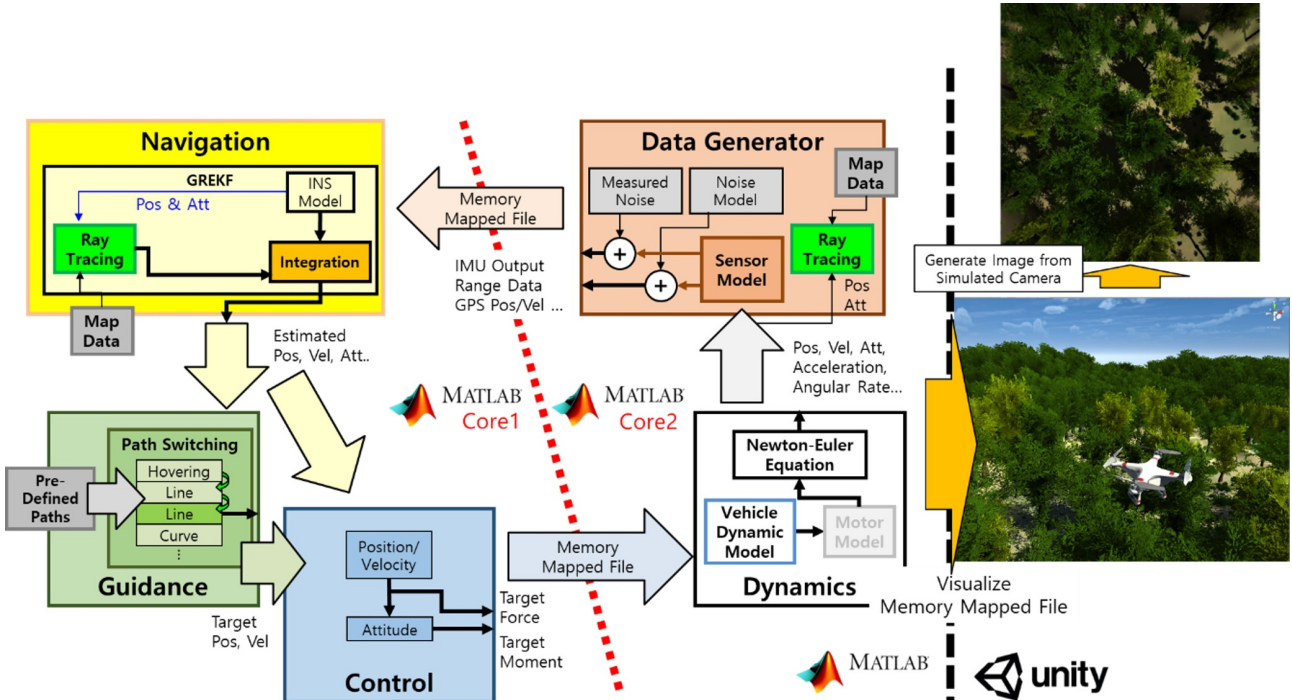


Fig. 9. Unity3D - MATLAB simulator block diagram.

the Unity3D engine-based simulator can provide a powerful inherent functions and framework that visualize the navigation results and simulate the image sensor.

The implementation of simulator is shown as in Fig. 9. In MATLAB and Unity3D, two processes operate independently. First, dynamics, sensor data generator, navigation, guidance, and control blocks in MATLAB run in a closed-loop manner by exchanging flight-related data. In the associated Unity3D environment, the drone flies over the virtual forest, in which image data are collected based on the true navigation results. The IMU, GPS, and barometer sensor data are generated using the drone's accurate

dynamic model and sensor measurement noise model. The ADIS16448's real sensor value was used by the IMU to model noise. Similarly, the GNSS sensor noise modeled using the real sensor value provided by the Novatel GNSS receiver. Then the INS/GPS loosely-coupled EKF computes the practical onboard navigation result through the artificial sensor measurements. The navigation result is, then, used for the drone's autopilot flight, which is conducted by thrust control of drone's dynamics along a pre-defined trajectory. In this way, the simulator can provide various validation dataset for the rescue mission by reflecting a real drone flight scenario.



Fig. 10. Referenced real vegetation environment image (upper) and simulated vegetation environment image in Unity3D (lower); left subplot depicts summer while right subplot depicts fall.

The AOS based survivor search proposed in this study is carried out by acquiring photos first from a drone's visible light spectrum using an RGB camera. So, in order to simulate a process that is similar to the real ones in the simulation environment, the artificial forest environment needs to mostly reflect the real forest vegetation. The assets in the Unity3D were used to replicate the forest environment in distinct temperate climates during summer and winter season as shown in Fig. 10. Real photo-based textures were applied to trees and the ground. And using the game engine's random tree generation and real-time shadow generation functions, a vegetation environment remarkably close to the real forest environment was created in the presented simulator.

Next, a number of avatars were placed in the previously created vegetation environment using the Ragdoll physics engine. The avatar with Ragdoll applied was struck down and lying on the ground in order to simulate the situation in which a real person stumbled. The environment in which the survivor in crisis is presented in Fig. 11, which was divided into four categories based on tree height and density.

The SAR mission is performed within a $64\text{ m} \times 64\text{ m}$ square search area. After taking off from the mission start area and entering the search area, the drone captures continuous images for the AOS, maintaining a 20-meter height within the search area. Fig. 12 shows the flight trajectory of drone and navigation result. The drone performs its own autopilot mission via the INS/GNSS/barometer LC EKF navigation, which is further used as image metadata. For data acquisition, a downward camera captures images in every 5-meter interval. Moreover, the camera was adjusted to FOV of 90 degrees in a square resolution of 1024×1024 pixels in the visible light spectrum, with



Fig. 11. Simulation environment with varied density of occlusion around survivors. (a) Fully occluded. (b) Half occluded. (c) Occluded with bush. (d) Open sky.

Table 1. Navigation in simulation RMSE.

Error	Hor.	Vert.	Roll	Pitch	Yaw
RMSE	0.41 m	0.2 m	0.06°	0.06°	0.61°

lens distortion and skew applied, as well as blurring effects due to focal distance and aperture diffraction to create more realistic images.

For the mission in Fig. 12, a total of 117 photos were generated during the simulation. The following is a comparison of genuine dynamics and navigation results. Table 1 summarizes the RMSE when comparing true dynamics and navigation outputs.

The simulation results for the human shape in the summer and autumn environment are shown as Figs. 13 and 14. In both scenarios, it was confirmed that when the AOS was performed using the true position of the camera, a person in distress was clearly detected, however when AOS was performed using a practical onboard navigation solu-

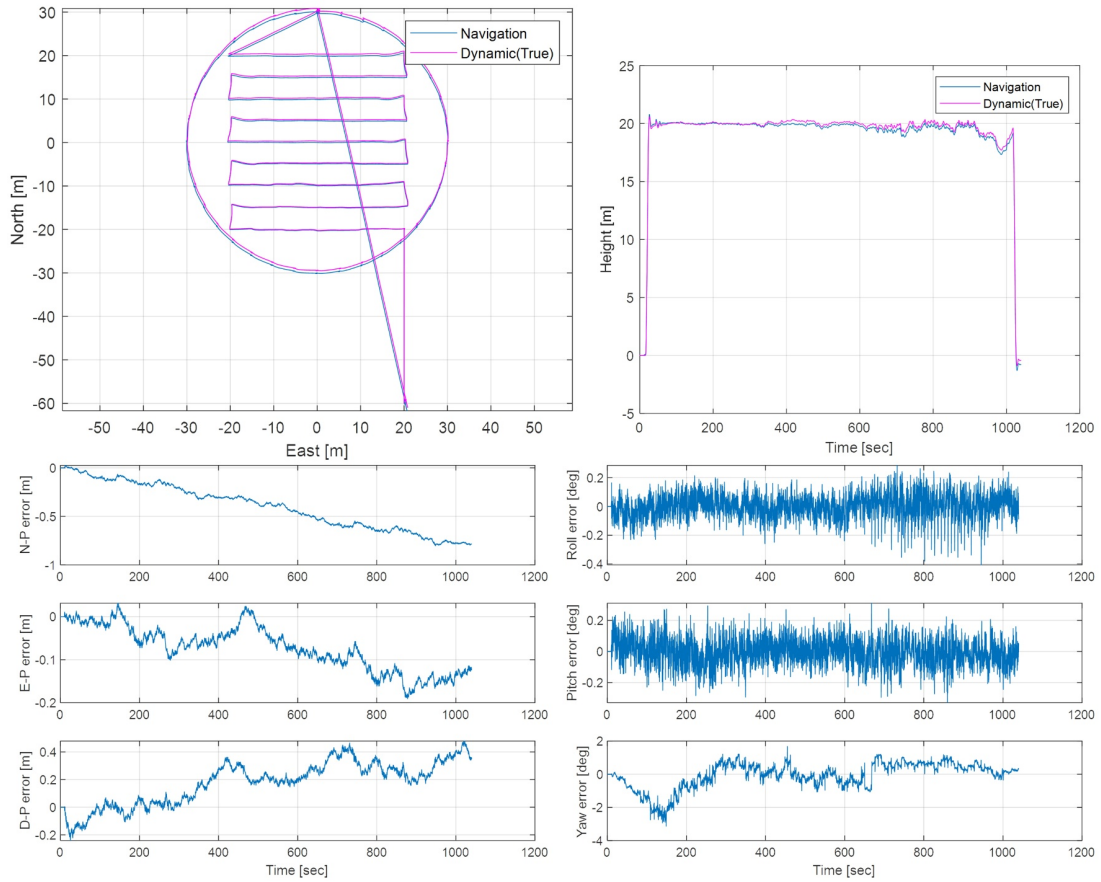


Fig. 12. Search and rescue simulation trajectory, navigation result and error.

tion, the shape of the person was crushed due to attitude and position errors. It does, however, remain a human-like appearance, making it easy to identify. In the fall environment, both RGB Only and HSV processed results revealed relatively good human shapes. But in the summer environment, there are many leaves. Therefore there are few photos of humans behind the leaves and photosynthesis is difficult because of the darkness that is caused by shadows while doing the AOS. So, the AOS result solely cannot reveal the survivors. However, as all the previously mentioned issues are resolved, the HSV-processed case validates the capacity of detection and identification of the troubled human form. As a result, the AOS can be successfully used even in visible light.

Now, the AOS result of the thermal image employed in the existing references [7,8] was compared to compare the performance of the proposed method. The task of recognizing the survivors was carried out using the same training weight profile, and the YOLO from the same reference was applied for a quantitative comparison. The human detector used is YOLov4-tiny, which was trained with thermal images and has a weight for real-time computations. So, the computing speed is fast, but the accuracy is not so good. The YOLO execution result of the AOS result based

on the actual thermal image data of reference [17] in Fig. 15(a) set as a comparison group also shows this characteristic. Although the AOS results of the standard thermal wavelength spectrum image show the human shape clearly and have no false positives or non-detection results, the YOLO confidence ranges variously from 20% to 75%, indicating a wide divergence and low accuracy. The YOLO results of the AOS results using the true pose were expressed in Figs. 15(b) and 15(c), respectively, and the YOLO results of the AOS results using the EKF Navigation pose were expressed in Fig. 15(e). In the figure, true positives are shown in green, false positives are in red, and undetected data are in yellow. Because the simulation used the same YOLO system as the comparison group (a), the total confidence is 8% to 70%, showing that the simulation functions well with the proposed HSV pre-processing method.

Figs. 15(c) and 15(e) show that the HSV pre-process removes all non-human components of the fall environment with fewer leaves and flat color, leaving only the survivors, which is recognized by YOLO, ensuring that there are no false positives or undetected parts. Furthermore, because the human element is simply left behind, classification performance is in the late 90% of APs, in-

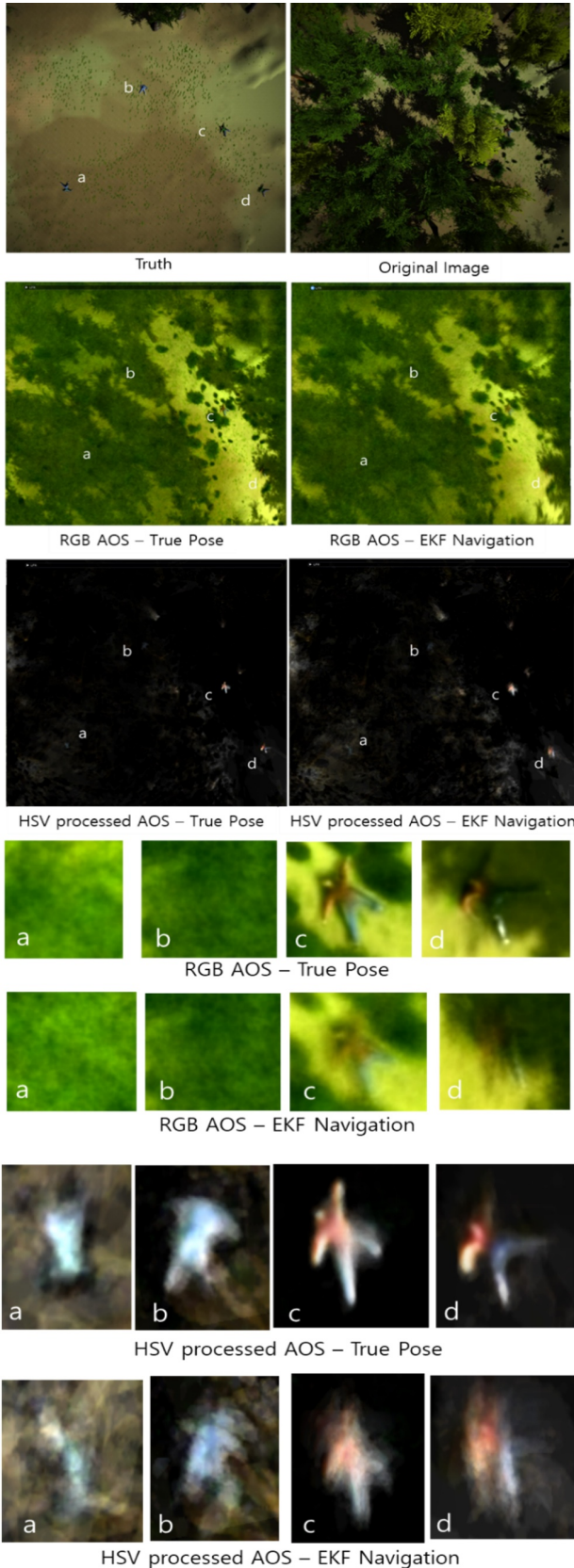


Fig. 13. SAR AOS simulation result - Summer. (a) Fully occluded. (b) Half occluded. (c) Occluded with bush. (d) Open sky.

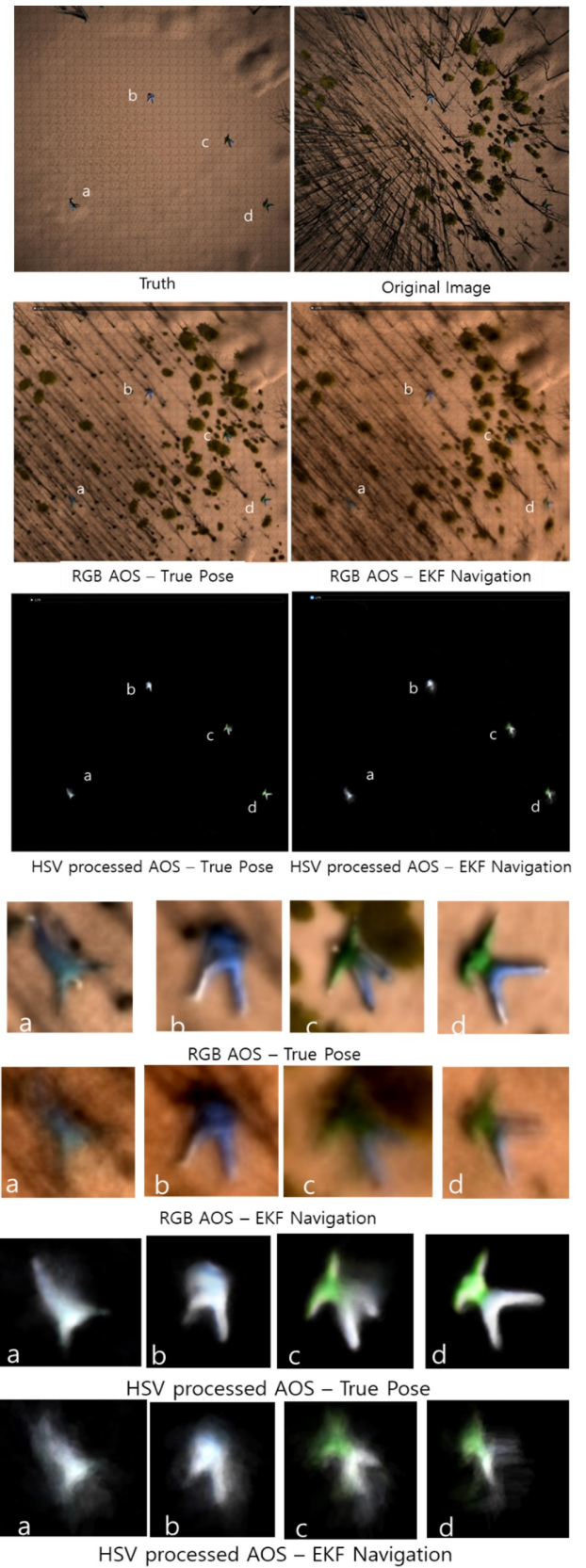


Fig. 14. SAR AOS simulation result - Fall. (a) Fully occluded. (b) Half occluded. (c) Occluded with bush. (d) Open sky.

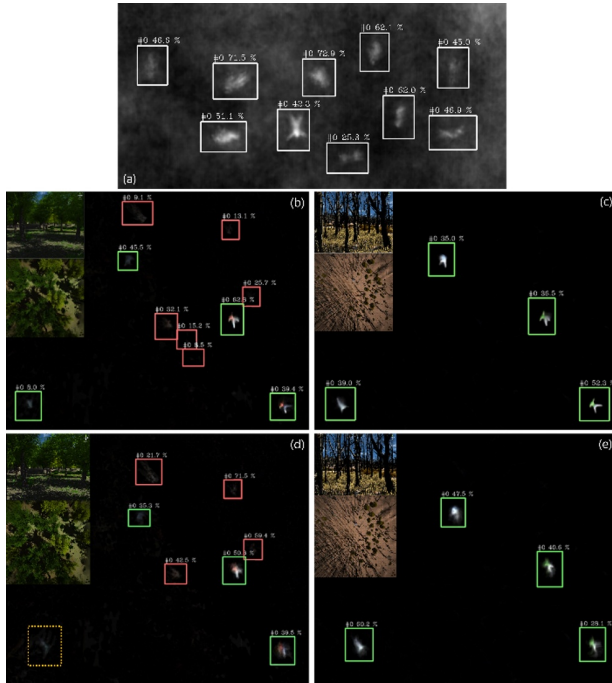


Fig. 15. SAR AOS YOLO result - true positive (green), false positive (red), not found (yellow). (a) JKU-ICG thermal AOS. (b) Simulation (summer) true pose. (c) Simulation (fall) true pose. (d) Simulation (summer) EKF navigation pose. (e) Simulation (fall) EKF navigation pose.

Table 2. AOS classification performance.

	Thermal	Visible spectrum (HSV processed)			
		Fall		Summer	
	JKU-ICG thermal (Ref.)	True pose	Nav. pose	True pose	Nav. pose
TP	631	296	297	243	193
FP	1	11	21	261	282
Total precision	99.8%	96.4%	93.4%	48.2%	40.6%
AP	91.0%	98.6%	98.8%	44.9%	31.0%

dicating very good accuracy as in the references. Green leaf components are not deleted in summer environments like (b) and (d) in Fig. 15, but parts like wooden columns and ground soles are detected as false positives. Survivors in a fully occluded environment may be considered less confident than in YOLO in the event of (d). This is also related to the fact that the total precision is approximated as 48.2% and 40.6%, respectively, when compared to the $TP/(TP+FP)$ ratio $4/10 = 40$ percent in Fig. 15(b) and the $TP/(TP+FP)$ ratio $3/7 = 42.86$ percent in Fig. 15(c), where the AP value is also 44.9% and 31.0%, respectively.

Table 2 and Fig. 16 show the average precision and PR-curve based on the image result in Fig. 15 and the quantitative result in [18].

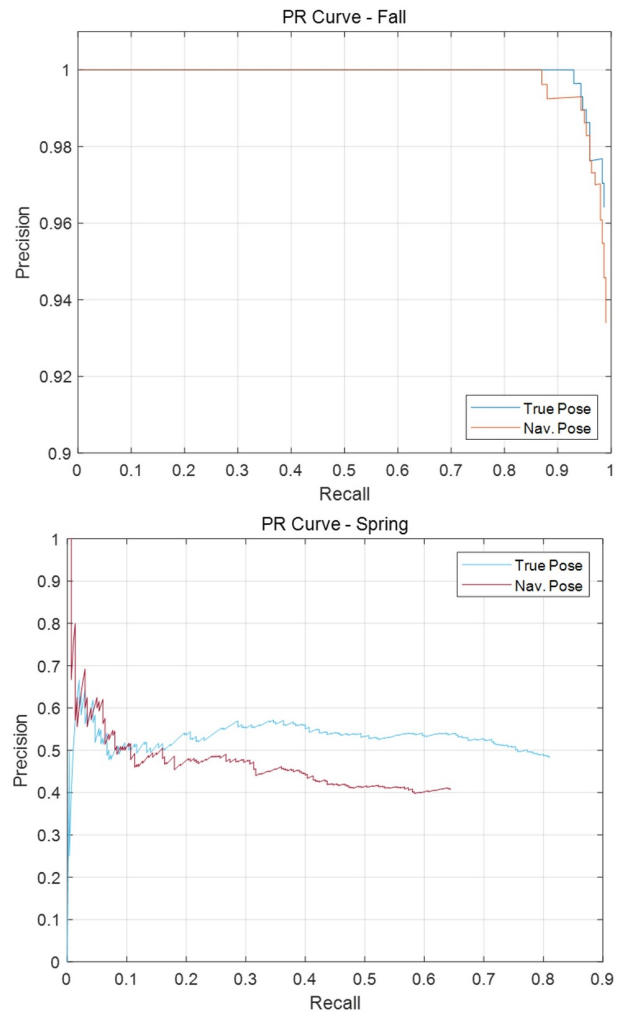


Fig. 16. Precision-recall curve.

Remark 1: Because the adapted YOLO algorithm is primarily trained for thermal images and was used to compare the results of this survivor detection to the referenced studies, there is a limitation that it cannot fully respond to the image in the visible light range employed in this paper. If the data in the visible wavelength range for YOLO training is adequately acquired through more study and the relevant weight is applied, it is expected that these false positives or non-detection difficulties would be overcome.

5. CONCLUSION

Through preprocessing in the HSV color space, this study demonstrated that the constraints of the existing visible light spectrum-based AOS can be overcome. Furthermore, image processing was handled using simple calculations rather than long and complicated algorithms, making it easy to use even when computations in a real-time embedded system are required. When designing an actual SAR drone system, these points can be used to en-

able SAR missions without the use of heavy and expensive thermal imaging equipment.

For algorithm verification, a high-fidelity hybrid simulator reflecting the real world environment was designed and quantitative performance comparison is presented. As experimental results can be varied with respect to different environmental conditions and simulator's model characteristics, the algorithm's robustness will be further evaluated in conjunction with experiment in future.

CONFLICT OF INTEREST

The authors declare that there is no competing financial interest or personal relationship that could have appeared to influence the work reported in this paper.

REFERENCES

- [1] J. M. D'Souza, V. V. Velpula, and K. R. Guruprasad, "Effectiveness of a camera as a UAV mounted search sensor for target detection: An experimental investigation," *International Journal of Control, Automation, and Systems*, vol. 19, pp. 2557-2568, 2021.
- [2] S. Shin, D. Min, and J. Lee, "Multi-matching-based vision navigation referencing map tile," *International Journal of Aeronautical and Space Sciences*, vol. 22, pp. 1119-1140, 2021.
- [3] M. Lee, S. G. Shin, S. Jang, W. Cho, S. Kim, S. Han, C. Choi, J. Kim, Y. Kim, and S. H. Kim, "Visual-based landing guidance system of UAV with deep learning technique for environments of visual-detection impairment," *International Journal of Control, Automation, and Systems*, vol. 20, pp. 1735-1744, 2022.
- [4] S. Kim, J. Park, D. Han, E. Kim, and D. Lee, "Development of a vision-based recognition and position measurement system for cooperative missions of multiple heterogeneous unmanned vehicles," *International Journal of Aeronautical and Space Sciences*, vol. 22, pp. 468-478, 2021.
- [5] I. Kurmi, D. C. Schedl, and O. Bimber, "Airborne optical sectioning," *Journal of Imaging*, vol. 4, no. 8, 102, 2018.
- [6] D. C. Schedl, I. Kurmi, and O. Bimber, "Airborne optical sectioning for nesting observation," *Scientific Reports*, vol. 10, Article number 7254, 2020.
- [7] D. C. Schedl, I. Kurmi, and O. Bimber, "Search and rescue with airborne optical sectioning," *Nature Machine Intelligence*, vol. 2, pp. 783-790, 2020.
- [8] I. Kurmi, D. C. Schedl, and O. Bimber, "An autonomous drone for search and rescue in forests using airborne optical sectioning," *Science Robotics*, vol. 6, no. 55, eabg1188, 2021.
- [9] I. Kurmi, D. C. Schedl, and O. Bimber, "Combined person classification with airborne optical sectioning," *Scientific Reports*, vol. 12, Article number 3804, 2022.
- [10] S. Sural, G. Qian, and S. Pramanik, "Segmentation and histogram generation using the HSV color space for image retrieval," *Proc. of International Conference on Image Processing*, 2002.
- [11] K. B. Shaik, P. Ganeshan, V. Kalist, B. S. Sathish, and J. M. M. Jenitha, "Comparative study of skin color detection and segmentation in HSV and YCbCr color space," *Procedia Computer Science*, vol. 57, pp. 41-48, 2015.
- [12] R. Cucchiara, C. Grana, M. Piccardi, A. Prati, and S. Sirotti, "Improving shadow suppression in moving object detection with HSV color information," *ITSC 2001. 2001 IEEE Intelligent Transportation Systems. Proceedings*, pp. 334-339, 2001.
- [13] T. F. Chan, S. H. Kang, and J. Shen, "Total variation denoising and enhancement of color images based on the CB and HSV color models," *Journal of Visual Communication and Image Representation*, vol. 12, no. 4, pp. 422-435, 2001.
- [14] X. Kong, "INS algorithm using quaternion model for low cost IMU," *Robotics and Autonomous Systems*, vol. 46, no. 4, pp. 221-246, 2004.
- [15] B. Lee, G. Park, K. Ryu, Y. J. Lee, and S. Sung, "Design of integrated navigation system using IMU and multiple ranges from in-flight rotating hexacopter system," *Proc. of IEEE/ION Position, Location and Navigation Symposium (PLANS)*, pp. 673-679, 2018.
- [16] E. Koh, G. Park, B. Lee, D. Kim, and S. Sung, "Performance validation and comparison of range/INS integrated system in urban navigation environment using Unity3D and PILS," *Proc. of IEEE/ION Position, Location and Navigation Symposium (PLANS)*, pp. 788-792, 2020.
- [17] D. C. Schedl, I. Kurmi, and O. Bimber. (2020). Data: Search and Rescue with Airborne Optical Sectioning [Data set]. Zenodo. <https://doi.org/10.5281/zenodo.4024677>
- [18] R. Padilla, S. L. Netto, and E. A. B. da Silva, "A survey on performance metrics for object-detection algorithms," *Proc. of International Conference on Systems, Signals and Image Processing (IWSSIP)*, pp. 237-242, 2020.



KangSoo Ryu received his B.S. degree in mechanical and automotive engineering from Seoul National University of Science and Technology, Seoul, Korea, in 2017. He is currently pursuing a Ph.D. degree in Konkuk University, Seoul, Korea, since 2017. His research interests include development of navigation, sensor fusion, and embedded systems for unmanned vehicles.

And he is currently expanding his area to digital-twin and simulation.



Byungjin Lee received his B.S. and Ph.D. degrees in aerospace engineering from Konkuk University, Seoul, Korea, in 2010 and 2017, respectively. He used to work for the Defense Agency for Technology and Quality, Korea. He has been continuing his research as a Research Professor at Konkuk University since 2020. His research interests include development of navigation and control system for unmanned vehicles, and he is currently expanding his area to sensor-level navigation systems.



Dong-Gyun Kim received his B.S. and M.S. degrees from the Department of Aerospace and Information Engineering, Konkuk University, Seoul, Korea, in 2014 and 2016, respectively, and a Ph.D. degree in 2023. He is currently a postdoctoral fellow at the same university. His research interests include robotic dynamics systems, unmanned intelligent systems, embedded software, path planning, and exploration.



Sangkyung Sung received his B.S. and Ph.D. degrees in electrical engineering from Seoul National University, Seoul, Korea, in 1996 and 2003, respectively. He worked for Samsung Electronics Co. Ltd., as a senior engineer before joining Konkuk University. Currently, he is a Professor of the Department of Aerospace Information Engineering at Konkuk University, Seoul Korea. His research interests include inertial sensor, integrated navigation algorithm, sensor fusion, embedded software, and application to mechatronics and unmanned autonomous systems.

Publisher's Note Springer Nature remains neutral with regard to jurisdictional claims in published maps and institutional affiliations.